Thrust and drag scaling of a rigid low-aspect-ratio pitching plate

Uwe Ehrenstein

Thrust and drag scaling of a rigid low-aspect-ratio pitching plate

Uwe Ehrenstein

Aix-Marseille Univ, CNRS, Centrale Marseille, M2P2, Marseille, France

Abstract

The flow around a rigid rectangular pitching plate immersed in a free stream is numerically investigated, addressing the force and drag generated by the oscillatory motion. Several aspect ratios (plate's span to plate's length) lower than 0.5 are considered, for a Reynolds number based on the plate's length and the incoming flow velocity of 2000. The validity of the scaling law for viscous drag production, previously established for finite-span plates in uniform flapping motion, is investigated for the pitching motion, which is more representative in the context of propulsion modeling. The time averaged pressure force is shown to decompose into a propulsive part, scaling linearly with the aspect ratio and induced by the plate's movement, and an opposite pressure force deficit, often interpreted as vortex induced drag and generally associated with the pair of longitudinal vortices at the plate's lateral edges. A scaling for the time averaged pressure deficit is proposed, by analyzing the pressure drop along the span in terms of a Bernoulli-type effect induced by the transverse flow velocity. It is shown, that the pressure thrust is reduced, compared to what would be predicted by the elongated body theory, by more than 30% for the aspect ratios considered.

Keywords: Swimming/flying, Propulsion

Email address: uwe.ehrenstein@univ-amu.fr (Uwe Ehrenstein)

1. Introduction

There has been an considerable amount of studies on the energetics of swimming over the past decades, parts of which having recently been reviewed in [1]. It appears that Lighthill's celebrated elongated-body theory [2] remains the key model for thrust prediction when addressing swimming or flying bodies, or when considering artificial systems for locomotion like oscillating foils, with relatively low aspect ratios (span to chord). The pressure field over the moving body or object characterizes the inertial fluid effects and for oscillatory motions, the tail-beat frequency as well as its amplitude has been widely used to characterize aquatic locomotion (see for instance [3, 4, 5] and references therein). For a freely swimming body, the thrust force is balanced by the resistive drag. Form drag depends on the swimming body's shape and at the same time the body's surface induces significant viscous forces, unless the Reynolds number range is sufficiently high such that viscous forces can be neglected.

The importance of viscous drag has been a matter of discussion and it has been recognized that the motion of finite-aspect swimming bodies or objects may induce a drag increase, due to what is known as the "Bone-Lighthill boundary-layer thinning hypothesis" [6]. This hypothesis has recently been readdressed for flapping plates and a longitudinal drag formula depending on the plate's aspect ratio, the wall-normal velocity induced by the plate's movement and of course the Reynolds number has been proposed [7, 8]. This friction law and in particular the finite-size scaling $\sim 1/\sqrt{s}$ with s the span of the foil is retrieved when modeling an actuated elastic swimmer [9]. Some discussion on the interaction between the surface of the body of swimming fishes and the induced boundary-layer flow is provided in [10]. Other observations however, for instance the measurements for the boundary layer on the body surface of trout swimming at high turbulent Reynolds numbers [11], do not support the boundary-layer thinning hypothesis, which is attributed to an energy-efficient swimming strategy in a turbulent environment.

The influence of the swimming object's aspect ratio on the inertial pressure

force is still not entirely elucidated. Scaling laws for propulsion for archetype geometries and motions, such as heaving, pitching or undulatory foils, often consider added-mass forces per unit span, which apply to rather large aspect ratio geometries, assuming a quasi two-dimensional setting along the foil's centerline. On the contrary, when addressing elongated bodies, the reactive term during the swimming motion is known to be proportional to the (small) width of the body. Reliable scaling laws have for instance been reported in [12], for a large aspect ratio (plate's span s to plate's length L) of $AR = s/L = 3.5$. The thrust-performance and the wake structure for rigid rectangular pitching plates have been reported in [13], providing evidence for quasi two-dimensional structures when $AR > 0.54$, whereas the aspect ratio affects the propulsive performance for narrower plates. Whatever aspect ratio is considered for three-dimensional oscillating foils or bodies in longitudinal motion, flow structures will evolve through the span, the manifestation being the generation of a pair of counter-rotating streamwise vortices at the lateral edges. These kind of structures are known as trailing vortices in wing theory, being responsible for what is often called induced drag. A vortex-induced drag model taking into account these streamwise vortex structures in undulatory swimming has been proposed in [14]. This model based on the vortex circulation is similar to the vortex drag analysis in [15]. Quite interesting, in this latter investigation it is mentioned, that an alternative interpretation would be to consider the pressure deficit due to the high transverse velocity between the vortex cores as responsible for the drag.

The aim of the present work is to characterize the influence of finite-size effects on the forces and drag for an oscillating archetype geometry, by computing the three-dimensional flow field induced by the motion. The numerical investigation is performed for a rigid pitching plate, considering different aspect ratios in the range of $1/8 \leq AR \leq 1/2$. The plate has vanishing thickness in this numerical solution procedure and hence form drag due to body shape is absent. The flow structure along the plate as well as in its the very vicinity is numerically captured and the instantaneous as well as time-averaged propulsive

and resistive forces can reliably be computed. The paper is organized as follows. In section 2, the numerical solution procedure is briefly outlined and the flow configuration and pitching parameters are addressed in section 3, together with some illustration of the three-dimensional flow structure. The forces and drag analysis is provided in section 4. The validity of the finite-aspect ratio viscous drag formula, derived for uniform motions, is examined for the pitching motion. The pressure force across the plate's span is analyzed and a scaling is derived for the pressure deficit. Finally, a scaling, function of the aspect ratio AR, is proposed for the pressure force, which takes into account the pressure deficit associated with the transverse flow. Some final discussion of the results is provides in section 5.

2. Numerical solution procedure

A multi-domain approach has been used for the solution of the Navier-Stokes system

$$\frac{\partial \mathbf{u}}{\partial t} + (\mathbf{u}\cdot\nabla)\mathbf{u} = -\frac{1}{\rho}\nabla p + \nu\nabla^2\mathbf{u}, \quad (1)$$

$$\nabla\cdot\mathbf{u} = 0, \quad (2)$$

for the velocity field $\mathbf{u} = (u, v, w)$ and the pressure p in the presence of the pitching plate. This approach has been already used for flapping plate computations in [8]. Also, the numerical approach, which will be briefly outlined hereafter, has been validated in [16] through comparisons with experimental measurements, for a pitching plate configuration in a quasi two-dimensional setting. A plate with vanishing thickness is considered and the domain partition is designed such that the edges of the plate coincide with contour lines of interfaces between subdomains. The mesh points associated with the singular plate's edges are hence shunned in the solution procedure, but they will nevertheless induce locally some noise in the gradients of the flow field. As the results will show, this noise is however smoothed out within small distances from the edges. The

flow domain in the three-dimensional coordinate system is

$$x_{in} \leq x \leq x_{in} + L_x,\ -L_y \leq y \leq L_y,\ -L_z \leq z \leq L_z. \tag{3}$$

In the numerical approach, motions of the plate are considered which can be described by a function $\eta(x,t)$ such that

$$y = \eta(x,t),\ x_l \leq x \leq x_t, -s/2 \leq z \leq s/2, \tag{4}$$

where x is the streamwise coordinate with x_l and x_t the plate's leading and trailing edge, respectively, y is the space coordinate normal to the incoming flow velocity (the plate is located at $y = 0$ in the absence of motion), s being the plate's width in the spanwise direction z. The pitching function used is

$$\eta(x,t) = (x - x_0)\alpha_0 \sin(2\pi f t),\ x_l \leq x \leq x_t, \tag{5}$$

where the pitch-pivot point x_0 has been chosen at the distance $L/3$ from the leading edge with $L = x_t - x_l$ the plate's length. For the motion (4) considered here the plate's leading and trailing edge x-coordinates are hold constant. This approximation with regard to the pitching motion is reasonable only for small pitching angles α_0 and the value $\alpha_0 = 10°$ has been considered, that is $\alpha_0 = \pi/18 = 0.175$. Note that although small, this pitching angle is within the range of investigations for pitching foils, for instance in [13] or very recently in [12]. The approximation of fixed leading and trailing edge x-coordinates may be interpreted as a small numerical stretching of the plate's length, which in the plate's maximal peak position takes the value $L\sqrt{1 + \tan^2(\alpha_0)} \approx 1.015\ L$ (that is a stretching of 1.5 percent).

The procedure uses a coordinate transformation which maps the physical coordinates into the computational ones. Denoting the computational variables with $(\bar{x}, \bar{y}, \bar{z})$, the coordinate transformation writes, according to the motion (4),

$$\bar{y} = \left(\frac{y - \eta(x,t)}{(\pm L_y) - \eta(x,t)} \right) (\pm L_y),\ x_l \leq \bar{x} = x \leq x_t, \tag{6}$$

for the domains $\eta < y < L_y$ and $-L_y < y < \eta$ respectively above and below the plate. Upstream the plate's edges the transformation writes similarly, by

replacing in (6) the function $\eta(x,t)$ with its values $\eta(x_l,t)$ and $\eta(x_t,t)$ at the leading edge and trailing edge, respectively.

In the transformed variables the plate is fixed at $\bar{y}=0$ and according to the transformation (6), the differential operators with respect to time t and the streamwise coordinate x can be decomposed, with

$$\frac{\partial}{\partial t}=\frac{\partial}{\partial \bar{t}}+\frac{\partial \eta/\partial t}{(\pm L_y)-\eta}(\bar{y}-(\pm L_y))\frac{\partial}{\partial \bar{y}},\ \frac{\partial}{\partial x}=\frac{\partial}{\partial \bar{x}}+\frac{\partial \eta/\partial x}{(\pm L_y)-\eta}(\bar{y}-(\pm L_y))\frac{\partial}{\partial \bar{y}}, \tag{7}$$

whereas the wall normal coordinate transforms as

$$\frac{\partial}{\partial y}=\frac{\partial}{\partial \bar{y}}+\frac{\eta}{(\pm L_y)-\eta}\frac{\partial}{\partial \bar{y}}. \tag{8}$$

The spanwise coordinate is of course unchanged for the motions such as (4). The

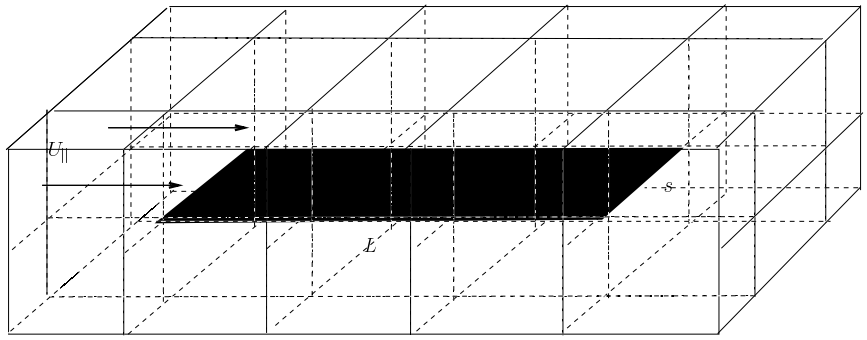

Figure 1: Sketch of the multidomain partition of the computational domain with the inserted plate (black). The dashed interior lines illustrate the subdomains' contours.

second order derivative operators are obtained accordingly and they are written as a sum of a Cartesian operator (in the computational variables) and the time-dependent contributions due to the metric terms. A semi-implicit second-order backward-Euler time integration is used, the metric term contributions of the differential operators as well as the nonlinear terms being evaluated explicitly through a Adams-Bashforth scheme. A projection method is considered, that is a fractional-step method by solving at each time step an intermediate pressure and velocity field followed by a pressure correction to ensure incompressibility, known as the Kim-Moin scheme (for a review on projection methods see [17]).

Hence, at each time step a series of Helmholtz-type problems

$$\bar{\nabla}^2\Phi - \sigma\Phi = f \tag{9}$$

for the velocity components and the pressure (with $\sigma = 0$ in the latter case) have to be solved. The domain $\Omega = \cup\Omega_k$ is partitioned into subdomains Ω_k with interfaces $\Gamma_{ij} = \Omega_i \cap \Omega_j$ (see the sketch in figure 1) and the Helmholtz problems in each subdomain are

$$\bar{\nabla}^2\Phi_k - \sigma\Phi_k = f_k, \text{ in } \Omega_k, \ \Phi_k = g \quad \text{on} \quad \partial\Omega_k \cap \partial\Omega, \tag{10}$$

where g is either an imposed boundary condition on the exterior of the whole computational domain, or a kinematic condition on the plate in the interior, depending on the specific subdomain considered. It is again emphasized that in this procedure $\bar{\nabla}$ is the Cartesian gradient operator, whereas the right-hand sides in (9), (10) contain the second order (in time) explicit evaluation of the nonlinear terms as well as the time-dependent metric terms.

High-order (8th order) compact finite differences schemes are considered for the discretization of the first and second order derivatives of the flow variables in the three computational space variables $(\bar{x}, \bar{y}, \bar{z})$. The schemes are derived for non-uniform meshes and in particular, as shown in [18], a clustering of the points near the boundary is appropriate for the eighth-order scheme considered here, to avoid oscillations and which enables a boundary closure scheme of the same order as the interior. Continuity of the solution as well as of its normal derivative is required at the domain interfaces Γ_{ij}. In [8] the algebraic formulation of this problem is outlined and it is explained, how the numerical algorithm involves the Schur complement matrix [19], also called influence matrix, its internal block structure being determined consistently with the subdomain partition in a pre-processing stage. A parallel *MPI* algorithm has been designed using the Cluster *IBM x3750* of the French computer center *IDRIS*, a process being assigned to each subdomain. The Schur complement system is solved iteratively using the *Portable, Extensible Toolkit for Scientific Computing (PETSc)* computational environment [20] and more specifically the *Krylov subspace package (KSP)*, using

hierarchical *GMRES* options and *Block Jocobi* preconditioning [20].

In all the computations, 384 subdomains have been considered, with $ndx = 12, ndy = 8, ndz = 4$ and in each subdomain Ω_k a $30 \times 30 \times 30$ mesh has been used. For a plate with length L, the inflow x_{in} of the computational domain has been set at a distance $L/2$ from the plate's leading edge and the domain's length in the streamwise direction is $L_x = 3L$ (that is the distance from the plate's trailing edge to the domain's outflow boundary is $3L/2$). The numerical approach has been used in [16], for similar flow conditions and equivalent plate motions, in however a quasi two-dimensional setting. In [16] the upper and lower flow domain boundaries have been varied from $\pm L_y = \pm 2L/3$ to $\pm L_y = \pm L$ and the overall computational domain's height could be shown to have only a weak influence on the stress tensor quantities along the plate. Here the upper and lower flow domain boundaries have been chosen at a distance $\pm L_y = \pm 3L/4$ and the results reported in [16], even though for two-dimensional flow, indicate that these boundaries are far enough from the pitching plate to minimize finite size effects. Free-surface flow boundary conditions are applied at the upper and lower boundaries $\pm L_y$ (that is zero Neumann boundary conditions for the steamwise u and spanwise w velocity components and a zero Dirichlet condition for the normal component v). In the spanwise direction $\pm L_z = \pm s$, that is the computational domain in z is twice as large as the plate. Periodic flow conditions have been considered at the domain's lateral boundaries in z. To assess the influence of the computational domain's width, a larger domain has also been considered for one of the plate's aspect ratios, by choosing $\pm L_z = \pm 3s/2$ and by imposing Dirichlet boundary conditions at the lateral boundaries of the enlarged computational domain. A brief comparison of the resulting flow field with that for the narrower domain will be provided in the next section. At inflow x_{in} the uniform incoming flow $(U_\parallel, 0, 0)$ is imposed and at the outflow $x = x_{in} + L_x$ non reflective advective outflow conditions have been used.

According to the plate's motion (4) with (5), the wall velocity is only in the y-direction and during the time-marching the kinematic boundary condition $u = 0, w = 0, v = \partial\eta/\partial t$ is applied for $x_l \leq \bar{x} \leq x_t, -s/2 \leq \bar{z} \leq s/2$, at the

moving plate located at $\bar{y} = 0$ in the transformed coordinate system $(\bar{x}, \bar{y}, \bar{z})$. It is recalled that the x-displacement during the pitching motion has indeed been discarded, which allows of the coordinate transformation (6). (As discussed above, this simplification may be interpreted as a small numerical stretching of the plate during its motion.) Note that for a perfect pitching motion, defining $\theta = \alpha_0 \sin(2\pi f t)$, the u-convection along the plate would approximately be $-(x - x_0)\sin(\theta)\, d\theta/dt$. This yields a highest u-convection amplitude in time, at the trailing edge and making dimensionless with $U_\parallel$, of approximately $\frac{2L}{3U_\parallel}\alpha_0^2 \pi f$. The frequencies considered here are such that $\frac{4L}{3U_\parallel}\alpha_0 f \leq 0.39$ (see next section) and the neglected u convection is hence smaller than 0.1 at the pitching angle of 10° considered. This has to be compared with the v-velocity at the plate, the highest dimensionless value (at the trailing edge) being approximately $\frac{4L}{3U_\parallel}\alpha_0 \pi f$, that is $2/\alpha_0 \approx 11.5$ higher than the highest u convection value.

3. Flow configuration and pitching parameters

All the following computations have been performed for a Reynolds number

$$Re_L = \frac{U_\parallel L}{\nu} = 2000, \tag{11}$$

$U_\parallel$, the incoming uniform flow velocity, and L the pate's length being the reference velocity and the reference length, respectively. The motion of the pitching plate with vanishing thickness is given by (4) with the pitching function (5) and for convenience, we set in the following $x_l = 0$ and hence the trailing edge $x_t = L$. It is recalled that the pitch-pivot point is at the distance $L/3$ from the leading edge, that is $x_0 = L/3$. The wall-normal velocity is according to (5)

$$U_\perp(x) = n_y \frac{\partial \eta}{\partial t} = n_y 2\pi\,(x - x_0)\, f\, \alpha_0\, \cos(2\pi f t), \tag{12}$$

where n_y is the y-component of the normal unit vector at the plate, that is

$$\mathbf{n} = \frac{\pm 1}{\sqrt{1 + (\partial\eta/\partial x)^2}}(-\frac{\partial \eta}{\partial x}, 1) = (n_x, n_y). \tag{13}$$

Note that given the relatively small pitching angle, $|n_y|$ is close to 1. The configuration is sketched in figure 2. Computations have been performed for

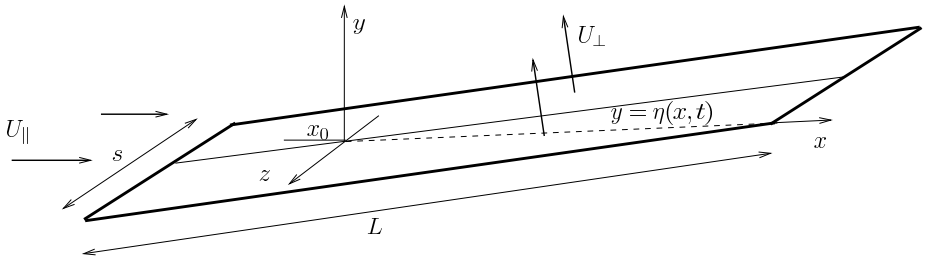

Figure 2: Sketch of the pitching plate with span s and length L in a uniform flow $U_\parallel$ moving at the normal velocity $U_\perp$.

different aspect ratios $AR = s/L$, with L the plate's length and s the plate's span, and various frequencies. In the following, the dimensionless variables are written with an asterisk $*$ (the plate's length L being the characteristic length and the incoming flow $U_\parallel$ the reference velocity). In the literature, the reduced frequency defined as $f^* = \pi f L/U_\parallel$ is often considered as the dimensionless frequency (sometimes without the factor π). Alternatively, the Strouhal number $St = Af/U_\parallel$ using the trailing edge peak-to-peak amplitude of motion A may be considered, which has been used widely to characterize in particular aquatic locomotion (see for instance [3] and more recently [5, 12]). Given the plate's motion (5), $A = (4/3)\alpha_0 L$ and hence $f^* = 0.75\, St\, \pi/\alpha_0$. The Strouhal number will be used throughout the paper and computations have been performed for $St = 0.23, 0.3, 0.39$ (or equivalently $f^* = 3.1, 4, 5.2$) and considering plates with different aspect ratios. Note that this range of Strouhal numbers is within the range of frequencies which is often associated with optimal thrust production (see [5] and references therein).

One has to be aware that the three-dimensional computations are rather time-consuming and that the simulations have to be performed beyond the transition regime in order to recover reliable mean quantities. Plate configurations with five different aspect ratios $AR = 1/8,\ 1/6,\ 1/4,\ 1/3,\ 1/2$ have been considered, for the two higher Strouhal numbers $St = 0.3, 0.39$, whereas for the lower Strouhal number $St = 0.23$ only the aspect ratios $AR = 1/6,\ 1/4$ have been considered. Note, that the lower the frequency, the longer the time in-

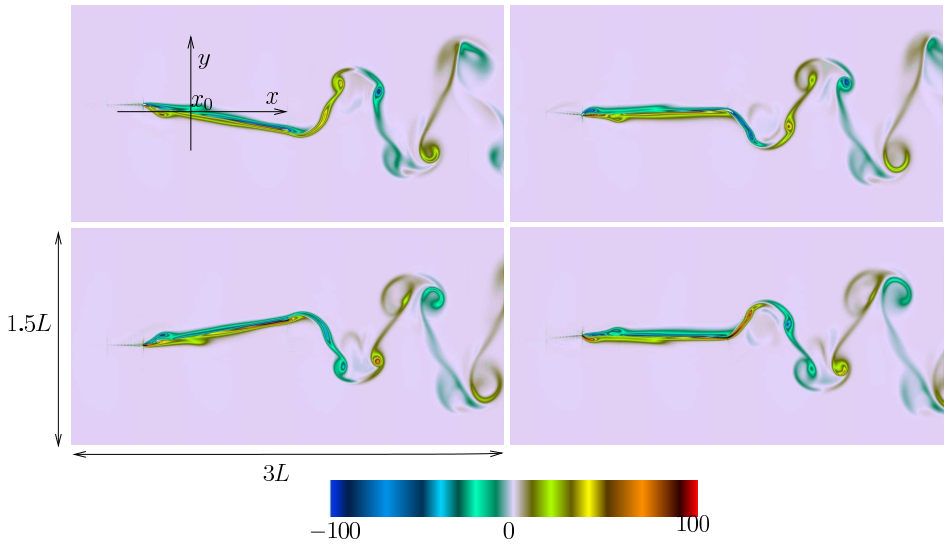

Figure 3: The instantaneous spanwise component ω_z^* of the vorticity in the plane (x, y) along the plate and in the wake, at the plate's center $z = 0$. Four positions during one period are shown: at the maximum lower pitching angle (upper left), close to the horizontal position in the upstroke movement (upper right), at the maximum higher pitching angle (lower left) and near the horizontal position in the downstroke movement (lower right). The pitching Strouhal number is $St = 0.3$ and the aspect ration $AR = 1/6$.

tegration has of course to be performed. An example of the flow dynamics is given in figure 3 which shows the spanwise component ω_z^* of the vorticity at the center of the plate $z = 0$. Four instantaneous flow fields are shown during one pitching period, for the Strouhal number $St = 0.3$ and the plate with the aspect ratio $AR = 1/6$. Note some spurious noise in the vorticity near the leading edge where the flow necessarily exhibits a singular behavior. The streamwise component ω_x^* of the vorticity in the plane (z, y) normal to the plate at $x = 0.75\,L$ is shown in figure 4, at the same instants in time during a pitching period as in figure 4. (Again, some noise in the vicinity of the singular lateral edges is visible.) The longitudinal vortices present at the lateral edges of the plate are similar to the so-called trailing vortices in the context of wing theory and have for instance been shown to contribute significantly to drag in bluff body theory [15]. It is seen that for the counter-rotating vortices, the vorticity magnitude (in

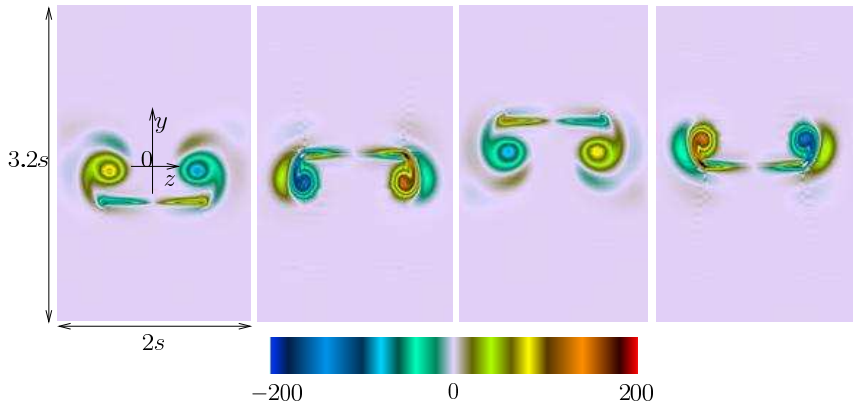

Figure 4: The instantaneous streamwise component ω_x^* of the vorticity in the plane (z, y) at a position $x = 0.75L$ on the plate, at the same instants in time during one pitching period as in figure 3, that is, from left to the right, the maximum lower position, close to the horizontal position in the upstroke movement, at the maximum higher pitching angle and near the horizontal position in the downstroke movement. The pitching Strouhal number is $St = 0.3$ and the aspect ratio of the plate is $AR = 1/6$. The different positions of the plate are those shown in figure 5 as the black horizontal line. Note that the domain area shown has been rescaled when comparing with figure 3 in order to emphasize the flow structure.

absolute values) is maximal when the plate is approximately in the horizontal position, which corresponds to the moment where the wall-normal velocity $|U_\perp|$ has its maximum. Note that the edge lines of the plate (recall that it has zero thickness), where the vorticity has a singular peak, are not explicitly resolved in the multi-domain solution procedure summarized in section 2.

As mentioned in the previous section, the computational domain in the spanwise direction z has been chosen twice as large as the plate and periodic boundary conditions have been applied at the spanwise boundaries of the computational domain. Periodic boundary conditions in the free-stream region at some distance of the plate are expected to put a minimum of constraints on the flow quantities along the plate. For one flow case, a spanwise domain three times as large as the immersed plate has been considered, with Dirichlet boundary conditions at the spanwise boundaries. The spanwise component w^* of the velocity field induced by the plate's motion in the plane (z, y) at $x = 0.75\,L$ for both the

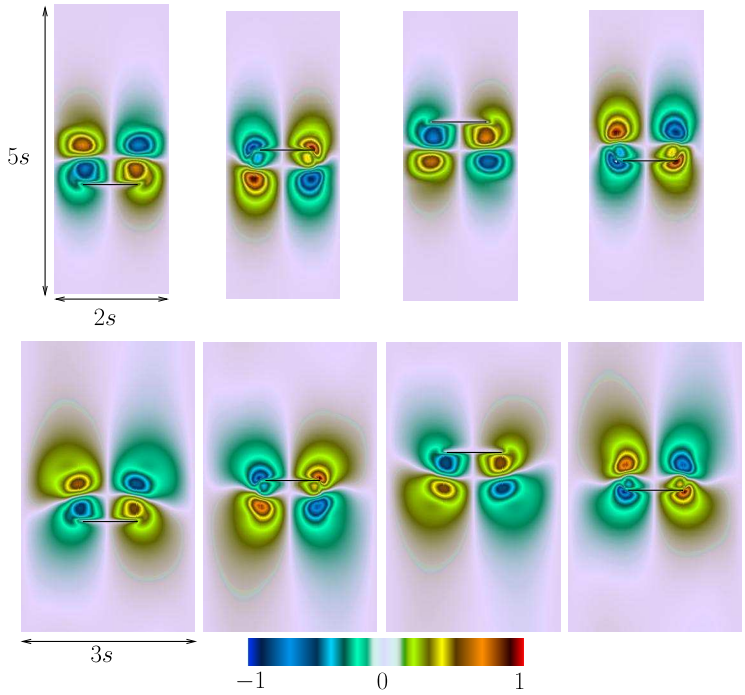

Figure 5: The instantaneous spanwise component w^* of the velocity field in the plane (z, y) at a position $x = 0.75L$ on the plate. Computational domain's width equal to $2s$ and with Neumann boundary conditions at the lateral boundaries (upper row), domain's width equal to $3s$ and with Dirichlet boundary conditions at the lateral boundaries (lower row). For each row, from left to right, at the plate's lowest position, close to the horizontal position in the upstroke movement, at the highest pitching angle and near the horizontal position in the downstroke movement. The different plate's positions are shown by the black line. The parameters are $St = 0.3$ and $AR = 1/8$.

computational domains is shown in figure 5 (for this comparison the aspect ratio $AR = 1/8$ has been considered). The snapshots shown in the upper row are those with the computational domain $-s \leq z \leq z$ and periodic boundary con-
260 ditions, whereas the lower row are those with $-3s/2 \leq z \leq 3s/2$ and Dirichlet boundary conditions. The spanwise velocity structure in the very vicinity of the plate (the position of which being marked as the black lines) looks very similar for both computational geometries. One observes that at the highest deviations from the horizontal position, where the wall-normal velocity tends to zero, the

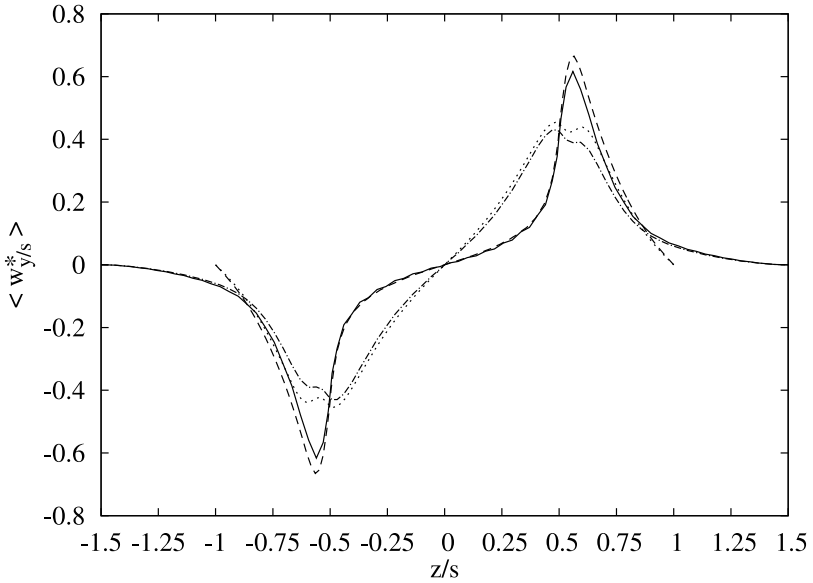

Figure 6: The time averaged spanwise velocity $< w^*_{y/S} >$ at position $x = 0.75L$ and at constant distances y/s from the plate, as function of z/s along the computational domain's width. Profile at the distance $y/s = 0.013$ with the large computational domain $-1.5 \leq z/s \leq 1.5$ and Dirichlet boundary conditions (_____) and with the narrower domain $-1 \leq z/s \leq -1$ and Neumann boundary conditions (_ _ _ _). Profile at the distance $y/s = 0.1$ with the large computational domain (_ . _ . _) and the narrower computational domain (. . . . .). The parameters are $St = 0.3$ and $AR = 1/8$ (the plate's lateral edges are at $z/s = \pm 0.5$).

spanwise velocity along the plate's windward-side approaches zero as well, as it can be inferred from the first and third snapshot (from the left) shown in figure 5. On the second and fourth snapshot, that is during the upward and downward motion respectively, spanwise velocity acceleration towards the lateral edges can be seen on the side to which the plate is moving. Also, the separation at the leeward-side of the plate is evidenced in the snapshots. A further comparison for both the computational domains is provided in figure 6, where the time averaged dimensionless spanwise velocity $< w^*_{y/s} >$ at two constant distances y/s relative to the moving plate are shown, as function of z/s. It is seen that the curves almost superimpose in the range $-0.5 \leq z/s \leq 0.5$ corresponding to the plate's span. For the larger computational domain, the spanwise velocity tends to zero with a vanishing gradient at the lateral boundaries $z/s \pm 1.5$. For the

narrower domain the periodic boundary condition applies and it is seen that w^* is close to zero at $z/s \pm 1$. The computational domain boundary constraint hence appears to have only a small influence on the spanwise velocity profile.

4. Forces and drag induced by the pitching plate

Before addressing the forces and drag computations, the main parameters which enter into the analysis are briefly summarized and a brief nomenclature of the drag force quantities is provided.

As mentioned before, the aspect ratio and the Strouhal number are

$$AR = s/L, \quad St = Af/U_{\parallel} \quad \text{with} \quad A = \frac{4}{3}\alpha_0 L. \tag{14}$$

In the forthcoming analysis, the dimensionless time-averaged wall-normal velocity is one of the key quantities, that is according to (12)) (taking $n_y = 1$)

$$\langle |U_{\perp}^*| \rangle (x^*) = \frac{3\pi}{2} St|x^* - 1/3| \frac{1}{T} \int_0^T |\cos(2\pi f t)| dt = 3St|x^* - 1/3|, \tag{15}$$

where $x^* = x/L$ and the dimensionless coordinate $x^* = 0$ corresponds to the plate's leading edge. The time-averaged thrust and drag forces are made dimensionless with $\rho U_{\parallel}^2 Ls$ and the dimensionless quantities are written with an asterisk $*$. The nomenclature used for the force quantities is (those with capital letter are time-averaged):

$\left\langle f_\mu^* \right\rangle (x)$	= spanwise integrated, time-averaged viscous stress,
F_μ^*	= total viscous drag,
$F_{\mu,th}^*$	= theoretical prediction for F_μ^*,
$\left\langle f_p^* \right\rangle (z)$	= streamwise integrated, time-averaged pressure stress,
$f_{pot}^*(z)$	= potential model for $\left\langle f_p^* \right\rangle (z)$,
$F_p^*(0)$	= pressure force based on centerline pressure,
$F_{p,th}^*(0)$	= prediction for $F_p^*(0)$ using elongated-body theory,
DF_p^*	= pressure force deficit due to finite span,
DF_{pot}^*	= potential model for DF_p^*,
$F_p^* = F_p^*(0) + DF_p^*$	= total pressure force,
$F_{p,scale}^*$	= scaling for F_p^*,
$F_{tot}^* = F_p^* + F_\mu^*$	= total force.

4.1. Skin friction formula revisited

Skin friction drag is likely to be considerably modified, with respect to the classical steady boundary-layer law, due to the compression of the boundary-layer when a finite-aspect ratio structure undergoes a flapping motion. This has been put forward by the 'Bone-Lighthill boundary layer thinning' hypothesis [6], which has recently been readdressed [7, 8] for a plate of width s in an external incoming stream velocity $U_\parallel$ moving perpendicularly to itself at a (constant) velocity U_p. We briefly outline how the skin friction enhancement in such a flow configuration can be understood. In the mid-plane $z = 0$ of the plate one finds, that the y component of the outer potential flow scales as $V_e \approx U_p(1 - y/H)$ with $H = s/2$ (see for instance [22] for potential flow calculations) for $y \ll s$. The fluid particles hence experience an acceleration $dU_e/dx \approx U_p/H$, with U_e the x component of the potential flow close to the wall. The resulting local viscous stress can be estimated (cf. [21]) and $\tau \approx \mu U_\parallel/\delta$ with $\delta \sim \sqrt{\nu s/U_p}$ the 'frictional boundary layer thickness' defined in [6]. Under the simplified hypothesis that this skin fiction enhancement is uniform along the span, one gets a theoretical scaling for the viscous drag induced by the plate's motion (L being the plate's length) $sL\tau \sim \mu U_\parallel L\sqrt{Re_s}\sqrt{U_p/U_\parallel}$, with Re_s the Reynolds

number formed with the plate's width s and $U_\parallel$. In [7] the complete three-dimensional problem in this configuration for a plate (of length L, span s and moving at a constant velocity U_p perpendicularly to itself) has been solved using the approximation of the momentum equations and taking also into account the acceleration of the fluid particles as they move around the plate. The resulting formula for the viscous drag is

$$F_{\mu,th} = C_{3D}\,\mu\,U_\parallel\,L\,\sqrt{Re_s}\sqrt{\frac{U_p}{U_\parallel}} \tag{16}$$

and when made dimensionless one gets

$$F^*_{\mu,th} = \frac{1}{\rho L U_\parallel^2 s}\,F_{\mu,th} = C_{3D}\,\frac{1}{\sqrt{Re_L}}\,\frac{1}{\sqrt{AR}}\,\sqrt{U_p^*} \tag{17}$$

with U_p^* the dimensionless wall-normal velocity (constant in the theoretical model), AR the plate's aspect ratio, Re_L being the Reynolds number using the plate's length L as reference length. The proportionality coefficient could be estimated in [8] as $C_{3D} \approx 1.8$.

For the present pitching plate, the wall-normal velocity is not constant any more along the chord of the plate. One may nevertheless hypothesize, that the skin friction induced by the plate's motion is somehow function of the velocity $U_\perp(x)$ given by (12). An example for the dimensionless local viscous stress for the Strouhal number $St = 0.3$ and the aspect ratio $AR = 1/6$

$$\tau^* = \frac{\mu}{\rho U_\parallel^2}\frac{\partial u_{|y=\eta}}{\partial y} \tag{18}$$

is depicted in figure 7, at the fixed position $x = 0.75\,L$ on the plate. The value at the upper face of the plate over two periods of pitching is shown. Two quantities are shown, that is the viscous stress at the plate's center $z = 0$ as well as the value averaged over the plate's span (integrating over the upper side of the plate) $\frac{1}{s}\int_{-s/S}^{s/2}\tau^*\,dz$. The (scaled) wall displacement is depicted as well. It is seen, that the periodic undulations of the centerline skin friction and of the spanwise-averaged quantity are similar, with however a shift in amplitude. The time-periodic skin friction evolution is seen to be more complex than a mere sinusoidal

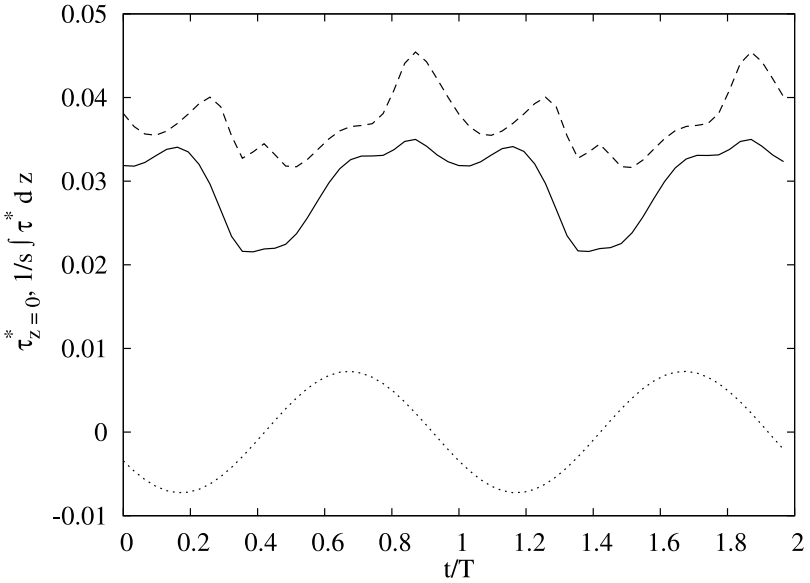

Figure 7: Local skin friction τ^* at $z = 0$ (_____) as well as the spanwise averaged viscous stress $\frac{1}{s}\int_{-s/S}^{s/2} \tau^* \, dz$ (_ _ _ _) over two pitching periods (for $St = 0.3$ and $AR = 1/6$), at $x = 0.75\,L$ on the upper the face of the plate. The scaled dimensionless wall displacement $(\eta^*(x = 0.75L, t))/10)$ is shown as well (.....).

oscillation. According to the theoretical formula (17), although strictly speaking valid for a constant velocity U_p^*, the time-dependent skin friction is expected to be reminiscent of the magnitude of the time-dependent wall-normal velocity. For instance, the plate's minimum positions after a downward movement (where the wall-normal velocity tends to zero) would than correspond to minimum values of the skin friction. A phase-shift is however observed, which can be attributed to the nonlinearities or more generally to a delay in the flow response to the wall movement.

As discussed in [7], the skin-friction enhancement is due to a compression of the boundary-layer, which however is not homogeneous in the spanwise direction, due to the acceleration of the fluid particles as they move around the plate. Four snapshots within one time period (at instants in time corresponding to figure 7 and at the same fixed $x = 0.75L$ location on the plate) of the skin friction along the span of the plate are shown in figure 8. The result for the steady state

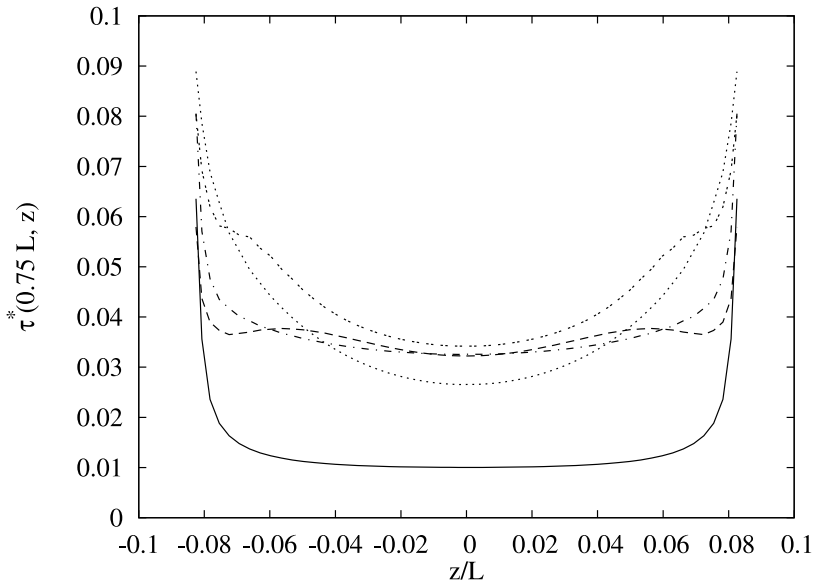

Figure 8: Instantaneous skin friction τ^* along the span $-AR/2 < z/L < AR/2$ (with $AR = 1/6$ and for pitching frequency $St = 0.3$) at $x = 0.75\,L$ on the plate, at $t/T = 0.065$ (_ _ _ _), $t/T = 0.29$ (.....), $t/T = 0.68$ (_._._._), $t/T = 0.9$ ((.. .. ..)(cf. figure 7). (_____) : result for the motionless plate.

along the motionless plate is also shown as the solid line and it is seen to be significantly smaller at $z = 0$ than the result for the pitching plate. Note that the Blasius formula $\tau^* = 0.332/\sqrt{Re_L(x/L)}$ (cf. [21]) predicts at this streamwise location $x = 0.75L$ a value $\tau^* \approx 0.0086$ which is indeed close to the computed value (at $z = 0$). Near the plate's lateral edges at $z/L = \pm AR/2 = \pm 1/12$, all curves exhibit a stiff increase in the very vicinity of this singular points. For the pitching plate, the skin friction more or less, depending on the instant in time, increases along the span which illustrates the friction enhancement when approaching the lateral edges at $z = \pm s/2$.

The stress tensor term along the plate has been computed, the x-component being

$$\sigma_x = \sigma_p + \sigma_\mu,\ \sigma_p = -p\,n_x,\ \sigma_\mu = 2\mu\frac{\partial u}{\partial x}\,n_x + \mu\left(\frac{\partial u}{\partial y} + \frac{\partial v}{\partial x}\right)\,n_y, \tag{19}$$

n_x and n_y being the x-component and the y-component of the normal-vector

(13). Here we consider the stress acting on the fluid by the plate, which means that the minus-sign is to be taken in (13) at the upper face of the plate and the plus-sign at the lower face. With this convention, a drag force on the plate is negative, which means that in the coordinate system sketched in figure 2, a positive total force corresponds in fact to thrust on the plate (which is the convention generally used). The skin-friction term at the wall $\tau = \mu \frac{\partial u_{|y=\eta}}{\partial y}$ is of course by far the dominant contribution to the viscous stress term σ_μ, for the pitching movement with a relatively small angle considered here. The time average of the dimensionless spanwise integrated viscous stress

$$< f_\mu^* > (x) >= \frac{1}{s\rho U_\parallel^2} \frac{1}{T} \int_{t_0}^{t_0+T} \left(\oint \sigma_\mu(x,z,t) dz \right) dt \tag{20}$$

has been computed, integrating at each position x the viscous stress along z on each side of the plate, using a simple trapezoidal rule in space and time, once a strictly periodic regime achieved. The results for three different aspect ratios $AR = 1/6, 1/4, 1/3$ and for the Strouhal number $St = 0.3$ are shown in figure 9. The portions of the plate near the leading and trailing edges, which are singular points in the solution procedure, have been omitted. Indeed, as already mentioned, near the plate's edges spurious oscillations of the mean quantities can hardly be avoided which however, as can be seen in the figure, do not affect the results along the major part of the plate. It is seen, that the lower the aspect ratio, the higher the viscous drag (its absolute value). The viscous drag for a higher Strouhal number $St = 0.39$ and $AR = 1/6$ is shown as well, which illustrates the increase of viscous drag with the pitching frequency. This appears to be in line with the theoretical friction force prediction (17), which however can only be derived rationally for a plate moving with constant and uniform velocity U_p^*. In the present pitching plate, the wall-normal velocity is periodic and depends on the streamwise location x. When trying to connect the computed time-averaged friction force to the theoretical formula, it seems natural to consider the time-average (15) of the wall-normal velocity, taking its absolute value, given that the upstroke and downstroke motion are equivalent for the overall drag production. Integrating this expression (17) along both the

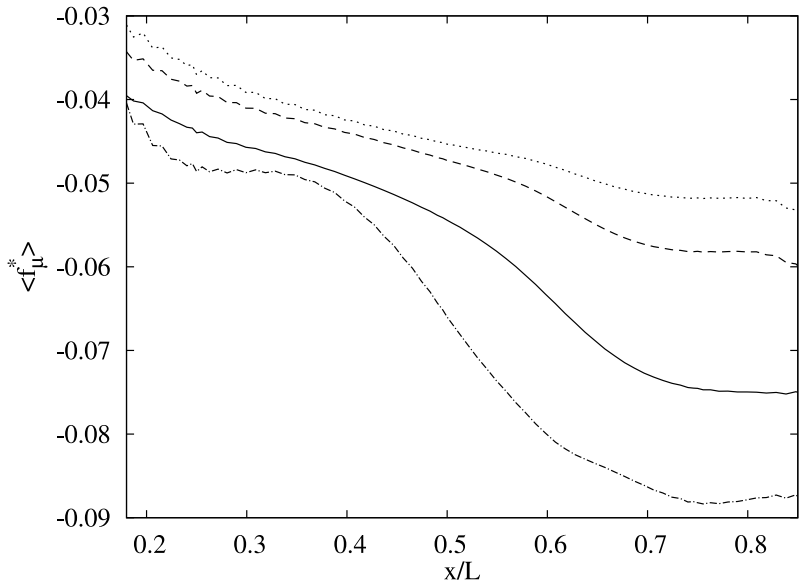

Figure 9: Dimensionless spanwise integrated and time averaged viscous stress $< f_\mu^* > (x)$ along the pitching plate oscillating at Strouhal number $St = 0.3$, for different aspect ratios $AR = 1/6$ (_____), $AR = 1/4$ (_ _ _ _), $AR = 1/3$ (.....). (_ . _ . _): $< f_\mu^* > (x)$ for $St = 0.39$ and $AR = 1/6$.

plate's sides, one gets $5\ St/3$ and it is hence supposed that

$$U_p^* \sim \frac{5}{3} St \tag{21}$$

(the sign $\sim$ indicating a factor of proportionality).

Taking this value in (17), the theory predicts

$$F_{\mu,th}^* = -C \frac{1}{\sqrt{Re_L}} \sqrt{\frac{St}{AR}} \tag{22}$$

(with the minus sign, according to the convention that drag is negative), where C is supposed to be more or less close to $C_{3D}\sqrt{5/3} \approx 2.3$ according to (17) (with $C_{3D} \approx 1.8$). For the different aspect ratios and frequencies, the dimensionless mean friction drag force

$$F_\mu^* = \frac{1}{L} \int_0^L < f_\mu^* > (x) > \ dx \tag{23}$$

has been computed, by integrating $< f_\mu^* > (x) >$ given by (20) along the plate from the leading edge to the trailing edge. Some simple trial and error for fixing

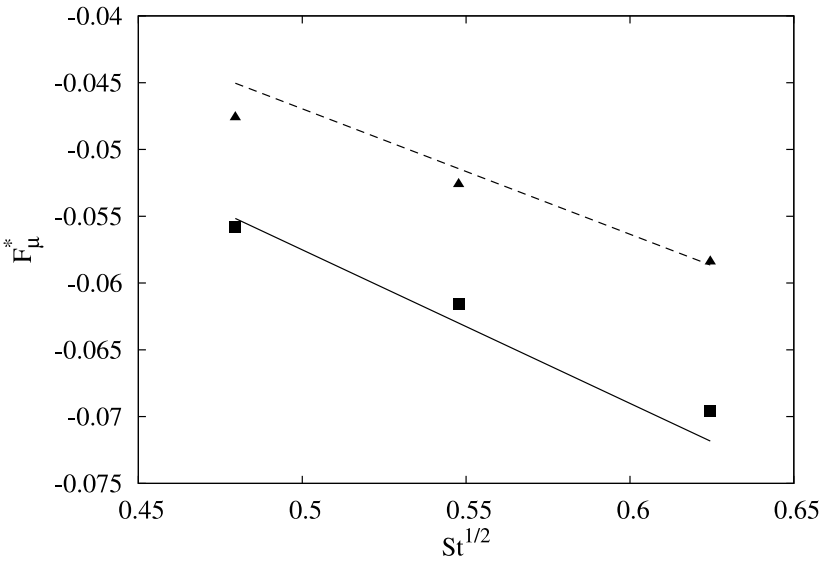

Figure 10: Dimensionless friction drag force F_μ^* for three Strouhal numbers $St = 0.23, 0.3, 0.39$ for the plate with aspect ratio $AR = 1/6$ (■) and the aspect ratio $AR = 1/4$ (▲). The straight lines correspond to the theoretical prediction $F^*_{\mu,th} = -2.1 \frac{1}{\sqrt{AR}} \frac{1}{\sqrt{Re_L}} St^{1/2}$ with $AR = 1/6$ (_____) and $AR = 1/4$ (_ _ _ _).

the factor C in the theoretical prediction (22) proved, that the value $C = 2.1$ fitted the best with the computed mean friction drag and the comparison is shown in figure 10. The friction drag force is depicted as function of $\sqrt{St}$, for the Strouhal numbers $St = 0.23, 0.3, 0.39$ and for two aspect ratios $AR = 1/6, 1/4$ as well as the theoretical prediction (22).

It is seen, that there is an almost linear dependence with respect to $\sqrt{St}$ for the three frequencies considered and the prediction (22) fits reasonably well for the the two aspect ratios considered. For the two higher frequencies $St = 0.3, 0.39$, simulations have been performed for different aspect ratios $AR = 1/8, 1/6, 1/4, 1/3$ and for the lower Strouhal number $St = 0.23$ for plates with $AR = 1/6, 1/4$. The resulting friction forces are shown by the square, triangle and dot symbols in figure 11, as function of $1/\sqrt{AR}$. Again, the lines corresponding to the theoretic value (22) are plotted as well. It is seen, that for $AR = 1/2$ (the largest aspect ratio considered) there is roughly a 30% difference

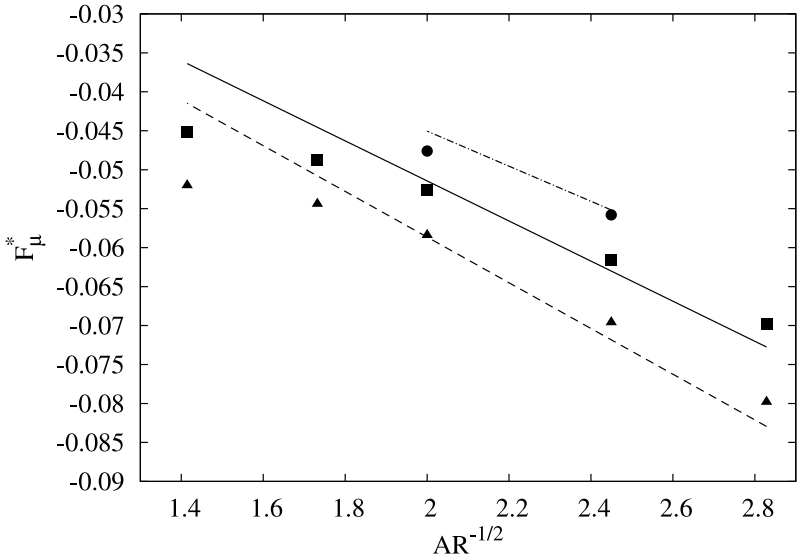

Figure 11: Dimensionless friction drag force F_μ^* as function of $AR^{-1/2}$ for aspect ratios $AR = 1/6, 1/4$ and Strouhal number $St_1 = 0.23$ (•) as well as aspect ratios $AR = 1/8, 1/6, 1/4, 1/3, 1/2$, Strouhal number $St_2 = 0.3$ (■), and Strouhal number $St_3 = 0.39$ (▲). The lines are the theoretical prediction $F^*_{\mu,th} = -2.1\sqrt{St_i}\frac{1}{\sqrt{Re_L}}\, AR^{-1/2}$ for St_1 (_ . _ . _), St_2 (_____), St_3 (_ _ _ _).

between the prediction and the computed friction forces, whereas for the lower aspect ratios $AR \leq 1/4$ the prediction and the computations are close. Indeed, the theoretical formula exploits the boundary-layer thinning phenomenon which is the dominant friction enhancement mechanism, only when the plate's span does not exceed some bound with respect to the plate's chord and for sufficiently high wall-normal velocities. Indeed, the total friction drag for a motionless plate is predicted by the Blasius formula (cf. [21]), the dimensionless value being $-1.33/\sqrt{Re_L} \approx -0.03$ (for $Re_L = 2000$). In figure 8 the computed value of the skin friction for the motionless plate with $AR = 1/6$ has also been shown. For this case the dimensionless total drag along the plate has been computed, yielding a value ≈ -0.036, that is a little higher drag than the theoretical Blasius prediction (which can mainly be attributed to the stiff increase of the local skin friction in the very vicinity of the lateral edges). Therefore, one can estimate according to the formula (22), that the wall-normal motion is certainly

the dominant drag production mechanism, as long as $C\sqrt{St/AR}$ is greater than 1.33. We have seen that $C \approx 2$ and $\sqrt{St/AR}$ is hence to be quite larger than roughly 0.5. For the Strouhal numbers considered here, this is the case for the aspect ratios $AR \leq 1/4$. Therefore, besides the case of small aspect ratios and high Strouhal numbers, where the theoretical prediction (22) is seen to be reliable, some combination between this formula and the classical flat-plate friction formula is to be taken (what is not attempted here, the paper rather focusing on small-aspect ratio aspects and relatively high pitching frequencies).

4.2. Pressure force across the plate's span

The dimensionless pressure $p^* = p/(\rho U_\parallel^2)$ has been computed along the plate and has been normalized such that $p^* = 0$ at inflow , where the pressure is expected to be almost uniform and it has been checked, that this is verified in the simulation results up to the order of 10^{-4} . The time evolution over two periods at a fixed location $x = 0.75\,L$ at the upper face is shown in figure (12). The scaled wall displacement is shown as well and again one observes a phase shift between the maximum and minimum values of p^* and those of the wall motion. The pressure value at the center $z = 0$ as well as the span averaged value $\frac{1}{s}\int_{-s/2}^{s/2} p^* dz$ are shown, and it is seen that they reach their maximum and minimum during the upstroke motion and downstroke motion, respectively, at instants a little shifted from the moments, where the plate is horizontal and the wall normal velocity is maximal. The gap between both curves indicates, that there is an overall loss of pressure along the span coordinate z.

Instantaneous pressure curves along the span at the upper surface at the position $x_p = 0.75L$ on the plate are shown in figure 13 during the upstroke motion, and in figure 14 during the downstroke motion. It is seen that during the upstroke motion the pressure variation along the span is rather strong, at least when the plate is not at its maximum position (which is equal to $x_p\alpha_0$). During the downstroke motion however the pressure at the upper face varies far less along the plate's span. Note that, according to the symmetry of the motion, the pressure at the lower face exhibits the inverse behavior (not shown

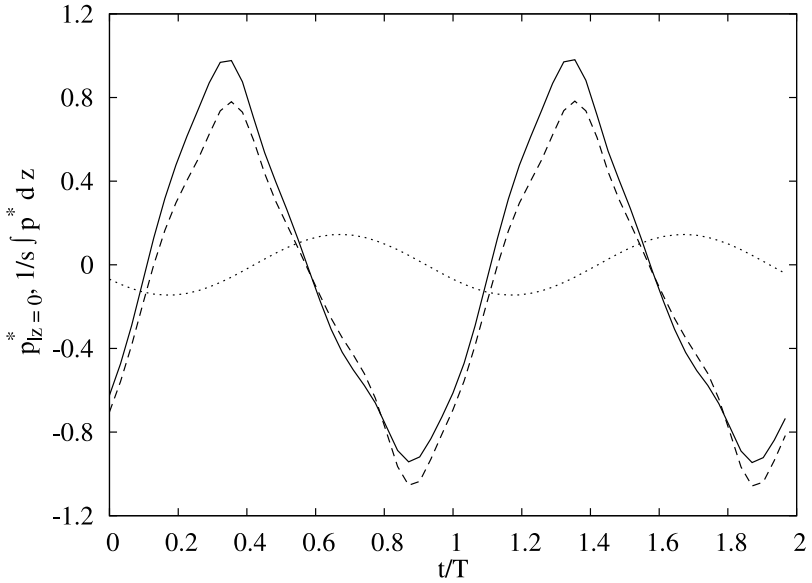

Figure 12: Dimensionless wall pressure p^* at $z = 0$ (_____) as well as the spanwise averaged pressure $\frac{1}{s}\int_{-s/S}^{s/2} p^*\,dz$ (_ _ _ _) over two pitching periods (for $St = 0.3$ and $AR = 1/6$), at $x = 0.75\,L$ at the upper face of the plate. The scaled dimensionless wall displacement ($2\eta^*(x = 0.75L, t)$) is shown as well (.....).

here), that is a strong variation along the span during the downstroke and a weak variation during the upstroke motion. The upstroke movement (respectively the downstroke movement) appears hence to be mainly responsible for the pressure variation along the span at the upper surface (respectively the lower surface).

The pressure evolution in z on the surface of the plate is certainly connected with the vortex structures at the plate's lateral edges. These vortex structures are intimately associated with the spanwise velocity w induced by the finite-width plate, which means that the pressure evolution and in particular its time-averaged value is also connected to the spanwise velocity. The velocity component is of course zero on the plate due to no slip. One may however assume that at some (small) distance from the plate, the computed spanwise velocity is reminiscent of a theoretical potential flow at the surface of a plate segment $-s/2 \leq z \leq s/2$ moving at a normal velocity U_p which is to be estimated. Supposing for the moment that this normal velocity is independent

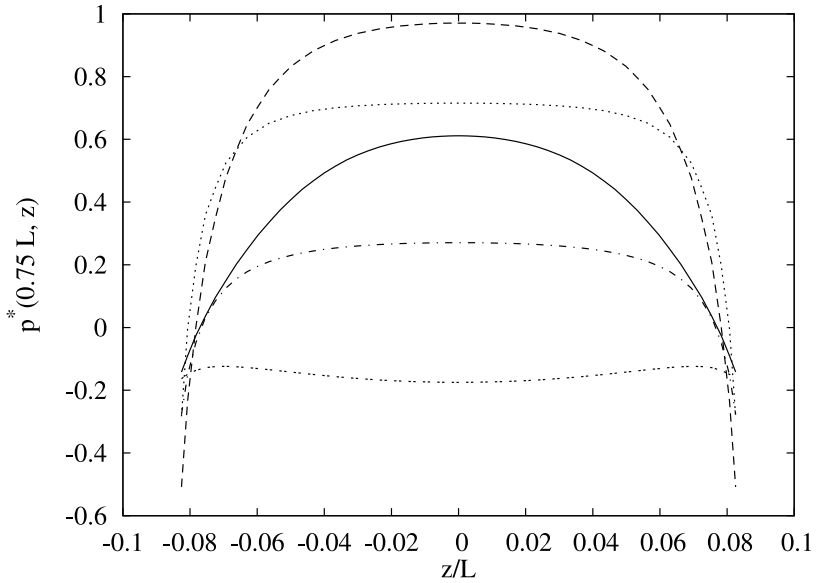

Figure 13: Instantaneous pressure distribution along the span $-AR/2 < z/L < AR/2$ (with $AR = 1/6$ and for pitching frequency $St = 0.3$) at $x_p = 0.75\,L$ on the upper face of the plate during the upstroke movement for the plate's position (the peak positions being $\eta = \pm x_p\alpha_0$) at $\eta = -0.95\ x_p\alpha_0$ (_____), $\eta = -0.6\ x_p\alpha_0$ (_ _ _ _), $\eta = 0$ (.....), $\eta = 0.56\ x_p\alpha_0$ (_._._), $\eta = 0.93\ x_p\alpha_0$ (.. .. ..).

of x and considering the plane (y, z), the potential velocity (v_{pot}, w_{pot}) can be found by use of the complex potential around a circle of radius $s/2$ together with the Joukowski transformation, which transforms the exterior of the circle into the exterior of the segment. This calculation can be found for instance in the textbook [22] and it has also been briefly recalled in [7]. This calculation yields

$$w^*_{pot} = \frac{U^*_p z}{\sqrt{(s/2)^2 - z^2}}, \tag{24}$$

for the theoretical spanwise potential velocity (made dimensionless with $U_\parallel$) component at the plate induced by a wall-normal velocity U^*_p.

The time averaged spanwise component $< w^*_{|y^*_c} >$ has been computed at distances y^*_c (made dimensionless with L) from the plate hold constant during the plate's oscillations, the result for $St = 0.3$ and $AR = 1/6$ being shown in figure 15. It can be seen, that at a small distance $y^*_c = 0.0016$, the velocity

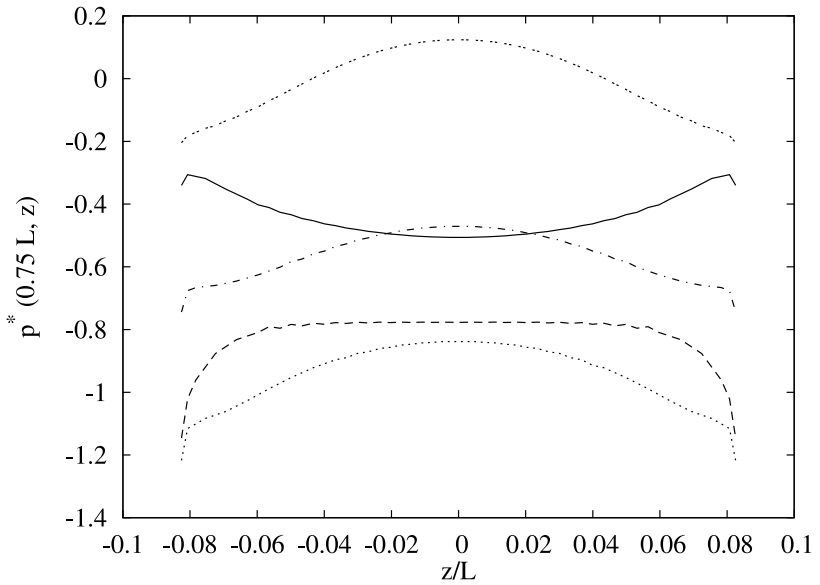

Figure 14: Instantaneous pressure distribution along the span $-AR/2 < z/L < AR/2$ (with $AR = 1/6$ and for pitching frequency $St = 0.3$) at $x_p = 0.75\,L$ on the upper face of the plate during the downstroke movement for the plate's position (the peak positions being $\eta = \pm x_p\alpha_0$) at $\eta = 0.97\ x_p\alpha_0$ (——), $\eta = 0.66\ x_p\alpha_0$ (– – –), $\eta = 0$ (·····), $\eta = -0.64\ x_p\alpha_0$ (– · –), $\eta = -0.96 x_p\alpha_0$ (·· ·· ··).

profile is rather flat due to the very vicinity of the plate (where no slip applies). However, at the three other distances $y_c^* = 0.0057, 0.013, 0.024$ the shapes of the velocity profiles are close.

Making a kind of locally parallel flow assumption in x, it is tempting to compare the spanwise velocity profile with the theoretical potential profile w_{pot}^*, considering the dimensionless wall-normal velocity U_p^* in (24) as to be proportional to the time averaged quantity (15), that is $U_p^* \sim 3St|x^* - 1/3|$. The solid curve in figure 15 corresponds to the dimensionless potential profile (24), avoiding of course the region near the edges where the potential velocity becomes singular, a proportional factor of 0.75 providing the best fit, that is $U_p^* = 0.94\,St$ (note that $x^* = 3/4$). Indeed, it is seen that, besides at $y_c^* = 0.0016$, that is very close to the wall where the no-slip condition is still reminiscent, the theoretical potential spanwise velocity fits well with the computed profiles.

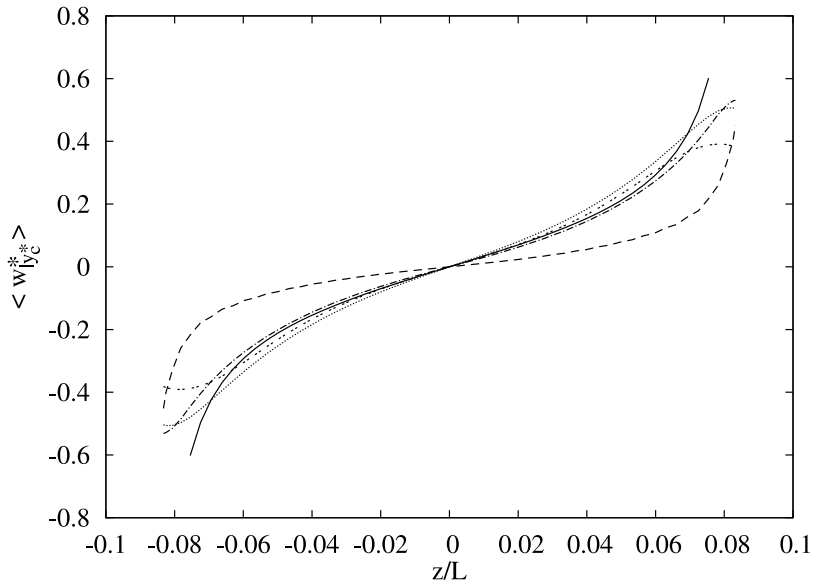

Figure 15: Mean spanwise velocity $< w^*_{|y^*_c} >$ along the span $-AR/2 < z/L < AR/2$ and at position $x = 0.75L$, at constant distances y^*_c from the plate (with $AR = 1/6$) during the motion (with pitching Strouhal number $St = 0.3$), with $y^*_c = 0.0016$ (_ _ _ _), $y^*_c = 0.0057$ (_ . _ . _), $y^*_c = 0.013$ (.....), $y^*_c = 0.024$ (.. .. ..). The potential velocity (24) with $U^*_p = 0.94St$ is depicted as well as the solid line (_____).

For the pitching motion with a relatively small pitching angle as considered in the present analysis, a reasonable hypothesis is to consider the pressure variation along the plate's span to be to some extent decorrelated from the (slower) streamwise evolution. One may hence assume a local (in x) Bernoulli-type assumption for the time-averaged pressure $< p^* >= \frac{1}{T}\int_{t_0}^{t_0+T} p^*\, dt$, that is

$$< p^* > (z) \approx < p^* > (z=0) - 0.5 < (w^*)^2 > (z) = p_{Bern}, \quad \text{at} \quad y = y_0, \quad (25)$$

with y_0 a fixed (small) distance from the plate.

Fixing $y^*_0 = 0.013$ as the small distance from the plate during the motion, the time averaged pressure and the Bernoulli assumption have been compared, with $< (w^*)^2 >$ the computed time-average of the square of the spanwise velocity component. An example of the computations is shown in figure 16, for the Strouhal number $St = 0.3$ and at the position $x = 0.75L$, for two aspect ratios $AR = 1/6, 1/3$. Even though the pressure distribution is not exactly repro-

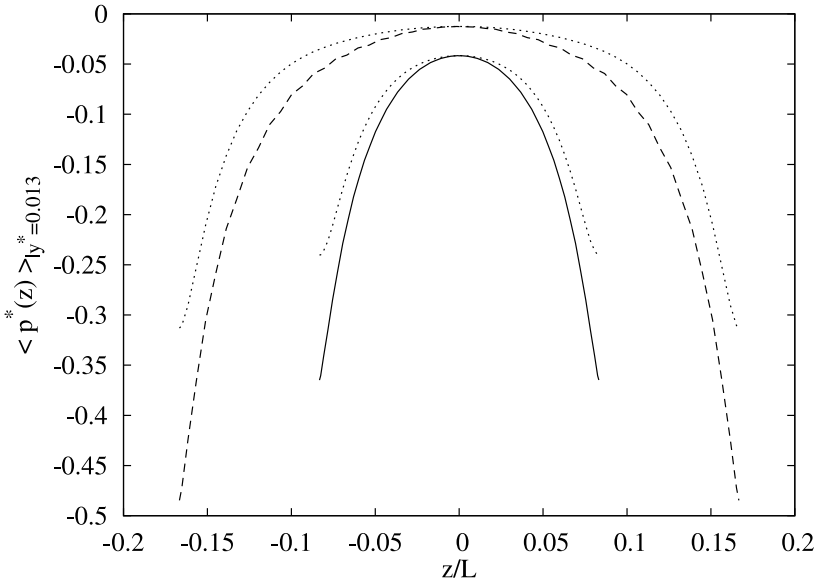

Figure 16: Mean pressure $< p^* >$ along the span at the distance $y_c^* = 0.013$ (hold constant during the plate's movement) from the plate and at the (dimensionless) position $x^* = 3/4$ from the leading edges, for the plate with $AR = 1/6$ (_____) and $AR = 1/3$ (_ _ _ _). The corresponding theoretical Bernoulli predictions $p_{Bern} =< p^* > (z = 0) - 0.5 < (w^*)^2 > (z)$ are superimposed (.....). The plate pitches at $St = 0.3$.

duced by the Bernoulli-type formula (25), the overall curvature of the pressure distribution is however captured, indicating the connection between the pressure deficit across the span and the spanwise velocity acceleration (here at a small distance from the plate).

4.3. Modeling of the pressure force deficit

The question is now, whether a Bernoulli principle is retrieved, when considering the streamwise pressure stress component $\sigma_p = -p\, n_x$ responsible for a possible thrust production, with n_x the x-component of the normal vector (13) on the plate. It is recalled that by convention, the vector $\mathbf{n}$ in (13) on the upper surface has the minus sign and the plus sign on the lower surface, in which case thrust on the plate corresponds to a positive pressure force in the present coordinate system. The pressure stress has been integrated in x along

the plate and the time average

$$< f_p^* > (z) = \frac{1}{T} \int_{t_0}^{t_0+T} \frac{1}{L} \int_0^L (-p^*)(x, z, t) n_x \, dx \, dt \tag{26}$$

has been computed. The result for the Strouhal number $St = 0.3$ and for the plate with different aspect ratios $AR = 1/8, 1/6, 1/4, 1/3$ is shown in figure 17. The integration in x has been performed at the plate's upper face, the same integration along the lower face providing of course identical results for the pitching motion. The spanwise bell-type shape of the pressure force seems indeed to be reminiscent of a Bernoulli effect, the pressure force decreasing from the center to a negative value close to -0.005 for the 4 aspect ratios considered.

To model this pressure force distribution along the plate's span, a decomposition

$$< f_p^* > (z) \approx f_{pot}^*(z) =< f_p^* > (z = 0) - 0.5 \, (w^{*2})_{pot}(z). \tag{27}$$

is sought and owing to the theoretical spanwise potential velocity (24) it is assumed that

$$(w^{*2})_{pot}(z) = \frac{(U^{*2})_p z^2}{(s/2)^2 a - z^2}. \tag{28}$$

The quantity $(U^{*2})_p$ is supposed to be proportional to the time and streamwise average of the square of the plate's normal velocity. According to (12) and taking $n_y = 1$, one gets the time-averaged quantity

$$\left\langle U_\perp^{*2} \right\rangle (x^*) = \frac{9\pi^2}{8} St^2 (x^* - 1/3)^2 \tag{29}$$

and integrating in x^* yields the value

$$(U^{*2})_p = C \frac{\pi^2}{8} St^2. \tag{30}$$

for a proportionality factor C. Also, a parameter a has been introduced in the expression (28), in the aim of fitting the pressure stress evolution along the span shown in figure and its value has been chosen as follows. Suppose that the $< f_p^* > (z = 0)$ at the center scales (for a fixed Strouhal number) roughly as the aspect ratio AR. This will be discussed later, but the figure already provides some evidence that the drop in the pressure force from the center to the edge

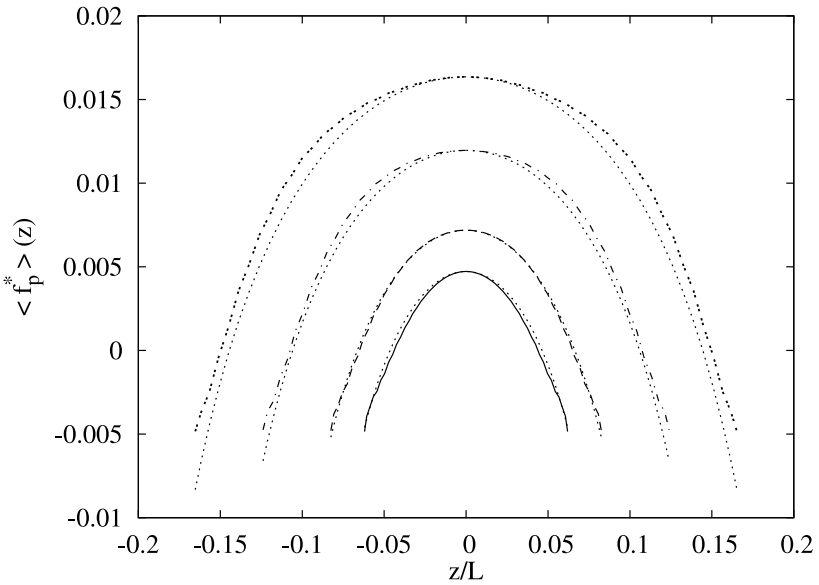

Figure 17: Mean pressure force distribution $< f_p^* > (z)$ along the plate's width z for different aspect ratios $AR = 1/8$ (——), $AR = 1/6$ (– – – –), $AR = 1/4$ (– · – · –) and $AR = 1/3$ (.. .. ..), for the pitching frequency $St = 0.3$. The potential model $f^*_{pot}(z) =< f_p^* > (z = 0) - 0.5\,(w^{*2})_{pot}(z)$ ($(w^{*2})_{pot}$ given by (28) with $(U^{*2})_p = 0.7\frac{\pi^2}{8}St^2$) is superimposed (.....) to the simulation results for the 4 aspect ratios.

is indeed roughly proportional to AR. If (27) holds, the parameter a in (28) is to be chosen such that at the plate's edges $\pm s/2$

$$0.5\,(w^{*2})_{pot}(\pm s/2) \sim AR \tag{31}$$

and according to (28), a is chosen such that $0.5\,\frac{(s/2)^2}{(s/2)^2 a-(s/2)^2} = AR$ and hence

$$a = \frac{1+2\,AR}{2\,AR}. \tag{32}$$

The potential model $f^*_{pot}(z)$ according to (27) with this value for a, by considering $C = 0.7$ in (30) as the proportionality factor, is superimposed in figure 17 as the dotted lines for the four aspect ratios. It is seen that the numerical simulation results and the potential model correspond surprisingly well.

The total pressure force F_p^* is now written as the sum of the centerline contribution, and the pressure force deficit due to the finite plate's width, that

is

$$F_p^* = \frac{1}{s} \oint < f_p^* > (z)\, dz = F_p^*(0) + DF_p^*, \tag{33}$$

($\oint$ meaning the integral over both plate faces), where $F_p^*(0) = 2 < f_p^*(z=0) >$ is the streamwise integrated dimensionless time averaged pressure force (26) at the centerline $z = 0$ of the plate (with the factor 2 for taking into account both plate's faces). According to (27)-(30), a potential model for the pressure force deficit DF_p^* can be derived, that is

$$DF_{pot}^* = -0.5 \oint (w^{*2})_{pot}(z)\, dz = -C\frac{\pi^2}{8} St^2 \frac{1}{s} \int_{-s/2}^{s/2} \frac{z^2}{(s/2)^2 a - z^2}\, dz. \tag{34}$$

The integration in (34) can easily be performed and

$$\begin{aligned} &\frac{1}{s} \int_{-s/2}^{s/2} \frac{z^2}{(s/2)^2 a - z^2}\, dz = \frac{\sqrt{a}}{2} \int_{-1/\sqrt{a}}^{1/\sqrt{a}} \frac{r^2}{1-r^2}\, dr \\ &= \frac{\sqrt{a}}{2} \left(\ln\left(1 + 1/\sqrt{a}\right) - \ln\left(1 - 1/\sqrt{a}\right) - 2/\sqrt{a} \right) \\ &= \frac{1}{3}\gamma + \frac{1}{5}\gamma^2 + \cdots \end{aligned} \tag{35}$$

with

$$\gamma = \frac{1}{a} = \frac{2\,AR}{2\,AR + 1}. \tag{36}$$

Expecting that the potential model mimics the general pressure force distribution, a scaling has been attempted keeping only the leading term $\frac{1}{3}\gamma$ in the expansion (35). Note that for the aspect ratios $1/8 \leq AR \leq 1/2$ considered, the parameter γ ranges from 0.2 to 0.5. Using the leading term of (35) in (34), the pressure force deficit resulting from the potential model is therefore estimated as

$$DF_{pot}^* = -C\frac{\pi^2}{24} St^2 \gamma \tag{37}$$

with again a coefficient C to be determined (which is expected to be of order of 1). For the different aspect ratios and frequencies considered, DF_p^* according to the decomposition (33) has been computed and the results are shown in figure 18 as function of γ. Again, simple trial and error for the proportionality factor C in (37) was performed and the coefficient $C = 0.8$ proved to be appropriate

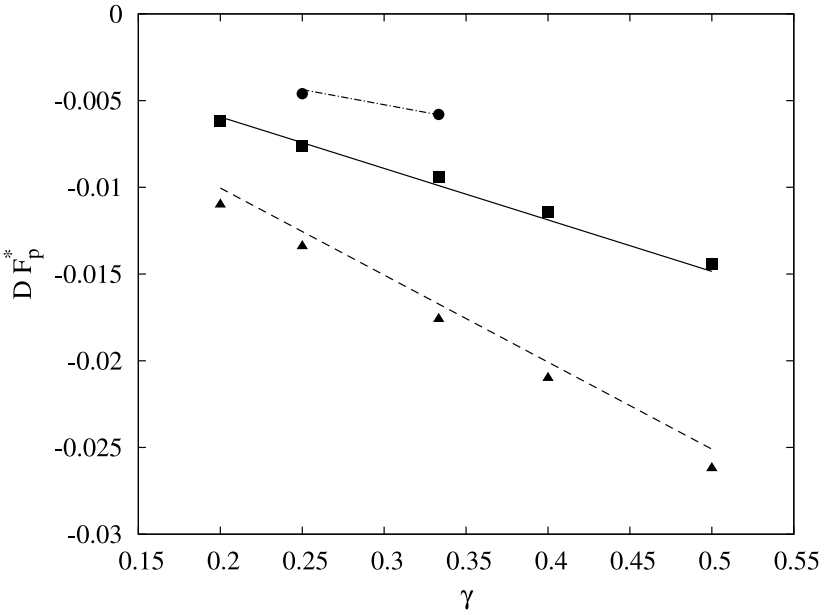

Figure 18: The pressure force deficit DF_p^* according to (33) as function of $\gamma = \frac{2\,AR}{2\,AR+1}$, for the Strouhal number $St_1 = 0.23$ and the aspect ratios $AR = 1/6, 1/4$ (●), as well as for $St_2 = 0.3$ (■) and $St_3 = 0.39$ (▲) and aspect ratios $AR = 1/8, 1/6, 1/4, 1/3, 1/2$. The lines are the theoretical prediction $DF_{pot}^* = -0.8\frac{\pi^2}{24}\,St^2\,\gamma$, for St_1 (_ . _ . _), St_2 (_____), St_3 (_ _ _ _).

for the prediction, as can be seen in figure 18, which provides indeed an evidence for the scaling (37).

Finally, a scaling for the thrust contribution due to the centerline pressure is to be undertaken. In the framework of elongated body theory (note that here the aspect ratio is relatively small), in [23] it has been pointed out, that thrust can be estimated by merely considering the motion of the swimming body's trailing edge, as long as the body cross section or lateral motion at the leading edge vanishes. As shown for instance in [9], the whole streamwise extension of the moving plate has however to be considered, when the added mass coefficient does not vanish at the leading edge, which is the case in the present pitching plate configuration with a pitch-pivot point at some distance from the leading edge. For thin oscillating plates and for purely potential flow, formulas for the reaction of the fluid accelerated by the body motion have been reviewed in [24]

and the formula

$$p_{th}(x,t) = \rho s \frac{\pi}{4} \left(\frac{\partial}{\partial t} + U_{\parallel} \frac{\partial}{\partial x} \right)^2 \eta(x,t), \tag{38}$$

is used, equivalent expressions having for instance been derived for added mass mechanisms in undulatory swimming in [25, 26]. For relatively small aspect ratios, the added mass is supposed to depend linearly on the plate's span (see for instance [27]) and according to the results in literature ([28]) the added mass coefficient $\rho s \frac{\pi}{4}$ is used here. By taking into account the plate's movement (5)

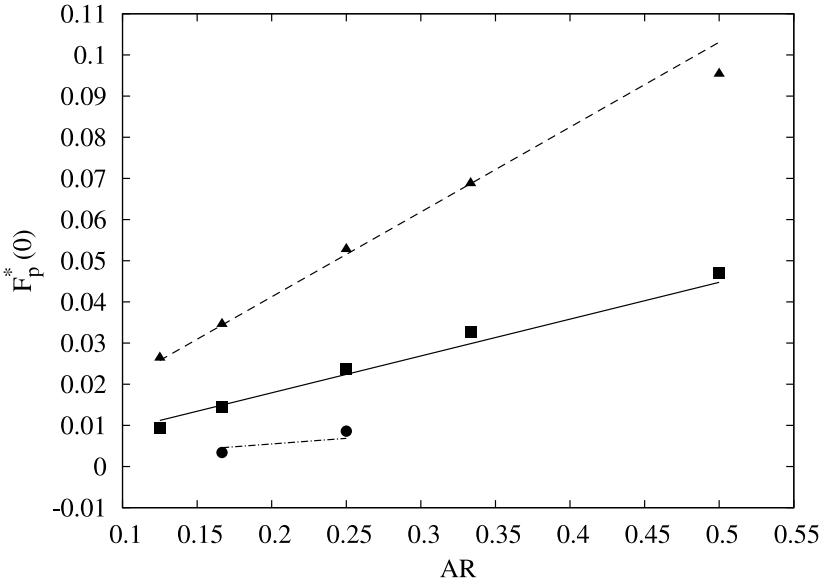

Figure 19: Centerline thrust $F_p^*(0)$ for aspect ratios $AR = 1/6, 1/4$ and Strouhal number $St_1 = 0.23$ (●) as well as aspect ratios $AR = 1/8, 1/6, 1/4, 1/3, 1/2$, Strouhal number $St_2 = 0.3$ (■), and Strouhal number $St_3 = 0.39$ (▲). The lines are the theoretical prediction $F^*_{p,th}(0) = AR\left(C_1 \frac{3\pi^3}{16} St_i^2 - C_2 \frac{3\pi^2}{2} St_i \alpha_0\right)$ with $C_1 = 0.44$ and $C_2 = 0.18$ for St_1 (_ _ _), St_2 (——), St_3 (_ _ _ _).

and the definition of the Strouhal number, one gets the following expression for the dimensionless streamwise integrated pressure model

$$P^*_{th}(t) = \frac{1}{\rho U_{\parallel}^2} \frac{1}{L} \int_0^L p_{th}\, dx = AR \left(-\frac{3\pi^3}{32} \frac{St^2}{\alpha_0} \sin(2\pi f t) + \frac{3\pi^2}{4} St \cos(2\pi f t) \right). \tag{39}$$

For the plate's pitching motion (5), the x-component of the wall's normal vector

$n_x \approx \partial\eta/\partial x = \alpha_0 \sin(2\pi f t)$ and one gets the scaling for the time averaged pressure force in the framework of elongated-body theory (considering the plate's upper and lower side)

$$F^*_{p,th}(0) = 2 < -P^*_{th}(t) n_x > = AR \left(C_1 \frac{3\pi^3}{16} St^2 - C_2 \frac{3\pi^2}{2} St \alpha_0 \right) \tag{40}$$

where C_1 and C_2 are the time-averages between the products of the trigonometric functions. It is expected that C_1 is close to 0.5, being the time-average of the square of the sinus function. The coefficient C_2 is the time-average of the product between a sine and a cosine function and is zero in theory, the functions being $\pi/2$ out of phase. As noted however for instance in [12], the fluid-plate dynamics will alter the phase differences between displacement and velocity or velocity and acceleration and terms which are expected to be $\pi/2$ out of phase may in fact develop in-phase components and C_2 is assumed to be nonzero. An

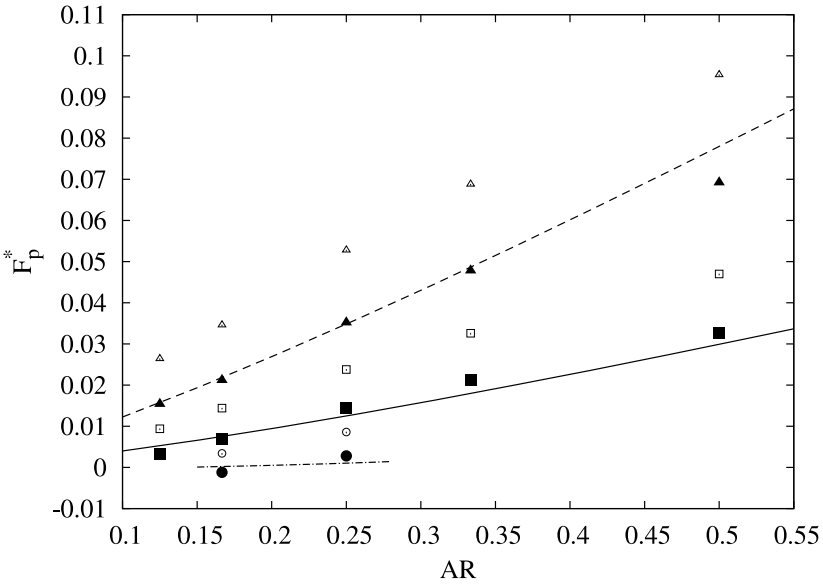

Figure 20: Thrust force F^*_p for aspect ratios $AR = 1/6, 1/4$ and Strouhal number $St_1 = 0.23$ (•) as well as aspect ratios $AR = 1/8, 1/6, 1/4, 1/3, 1/2$, Strouhal number $St_2 = 0.3$ (■), and Strouhal number $St_3 = 0.39$ (▲). The lines are the theoretical prediction $F^*_{p,scale} = AR \left(C_1 \frac{3\pi^3}{16} St_i^2 - C_2 \frac{3\pi^2}{2} St_i \alpha_0 \right) - \frac{2\,AR}{2\,AR+1} C_3 \frac{\pi^2}{24} St_i^2$ with $C_1 = 0.44$, $C_2 = 0.18$ and $C_3 = 0.8$, for St_1 (_ . _ . _), St_2 (_____), St_3 (_ _ _ _). The centerline thrust prediction of figure 19 are depicted as the empty symbols.

equivalent scaling as in (40) has been proposed recently in [12] and propulsive pressure force scaling in the presence of undulating elastic plates, within the elongated-body theory of Lighthill [6], are discussed in [9].

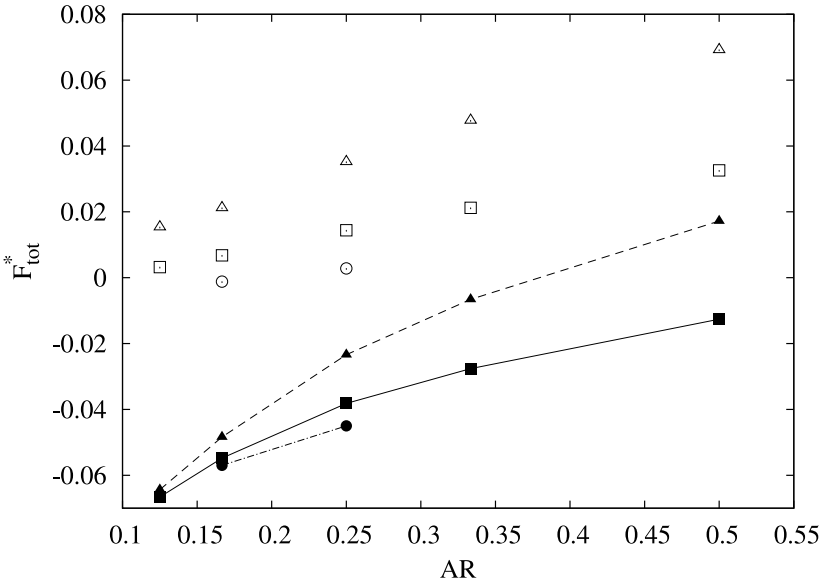

Figure 21: The total force $F^*_{tot} = F^*_p + F^*_\mu$ as function of AR, for aspect ratios $AR = 1/6, 1/4$ and Strouhal number $St_1 = 0.23$ (●) as well as aspect ratios $AR = 1/8, 1/6, 1/4, 1/3, 1/2$, Strouhal number $St_2 = 0.3$ (■), and Strouhal number $St_3 = 0.39$ (▲). The pressure thrust force values F^*_p of figure 20 are depicted as the empty symbols.

.

The centerline mean dimensionless pressure force $F^*_p(0)$ according to the decomposition (33) has been computed and has been compared with the theoretical prediction (40), for appropriately chosen coefficients C_1 and C_2, which again are found by simple trial and error fitting (starting with the theoretical value $C_1 = 0.5$ and small C_2), yielding $C_1 = 0.44$ and $C_2 = 0.18$. The results are shown in figure 19, again for the Strouhal numbers $St = 0.3, 0.39$ and the aspect ratios $AR = 1/8, 1/6, 1/4, 1/3, 1/2$ and also for $St = 0.23$ (and $AR = 1/6, 1/4$). The simulation results are shown as the symbols in figure 19. The theoretical expression $F^*_{p,th}(0)$ in (40) is plotted as well for the three Strouhal numbers.

It is seen, that the curves fit quite nicely with the computed values, those for $AR = 0.5$ and $St = 0.39$ being however a little off. This is not surprising, given that the theoretical loading (depending linearly on AR) is only reliable for rather low aspect ratios (see for instance [26]).

The total pressure force F_p^* according to the decomposition (33) is depicted in figure 20 for the different aspect ratios and Strouhal numbers as the black symbols (the centerline thrust values of figure 19 are depicted as the empty symbols to illustrate the loss in thrust). The total thrust force scaling taking into account the approximation (37) for the pressure force deficit is

$$F^*_{p,scale} = AR\left(C_1\frac{3\pi^3}{16}St^2 - C_2\frac{3\pi^2}{2}St\,\alpha_0\right) - \frac{2\,AR}{2\,AR+1}C_3\frac{\pi^2}{24}\,St^2 \qquad (41)$$

with $C_1 = 0.44, C_2 = 0.18, C_3 = 0.8$ and this function is depicted as well. It is seen, that this formula represents fairly well the computed values. It is important to note, that the Bernoulli type effect diminishes the pressure thrust force, as predicted by the elongated body theory with a scaling $\sim AR$, by about 40%, for $AR = 1/8$ and by roughly 30% for $AR = 0.5$, for the highest Strouhal number $St = 0.39$ considered.

The total force $F^*_{tot} = F^*_p + F^*_\mu$, that is the sum of the pressure thrust force and the friction drag force, is shown in figure 21. The pressure thrust force F^*_p results of figure 20 are also shown as the empty symbols to emphasize the loss of performance due to the viscous drag. Indeed, for the range of aspect ratios and for the Reynolds number $Re_L = 2000$ considered, only the pitching plate with the highest Strouhal number $St = 0.39$ produces net thrust for $AR > 1/3$.

5. Concluding discussion

The precise force balance for a pitching plate has been extracted from three-dimensional numerical simulation results, for plates with different and relatively small aspect ratios (span to length) $AR = s/L$ and for different Strouhal number $St = Af/U_\parallel$ (with f the frequency, A the maximum trailing edge amplitude and $U_\parallel$ the incoming flow velocity). The Strouhal numbers considered are in

the range $0.2 < St < 0.4$ which for instance is typical for a large number of fish [29].

A theoretical skin friction model, which had been derived for uniform finite-span plate motions, has been shown to provide also a satisfactory friction scaling (for a given Reynolds number) $F_\mu^* \sim \sqrt{St/AR}$, even though the wall normal velocity evolves along the streamwise direction of the plate, the moderate pitching angle considered limiting the streamwise gradients.

The lateral edge vortices (or trailing vortices) inevitably appear during the propulsion of a finite-span object. Attempts have been made to quantify the resulting vortex induced drag (for a very recent discussion, see [1]). Making however in the present work the assumption that the key-quantity for this pressure force deficit is the more or less high transverse velocity between the counter-rotating trailing vortices, it has been attempted to interpret the time-averaged pressure deficit in terms of a Bernoulli-type effect. The potential model for the spanwise velocity of an oscillating finite-span plate could be tuned to reproduce the averaged pressure force distribution along the span and a scaling of the pressure force deficit $\sim -St^2\, 2AR\,/(2AR+1)$ has been shown to be reliable for the different aspect ratios and Strouhal numbers considered. The scaling (41) proved to fit the computed non-dimensional pressure force $F_p^* = F_p/(\rho U_\parallel^2 Ls)$, the classical mean propulsive force scaling for slender-body swimmers proportional to AR being corrected by the pressure drag. According to this composite scaling, the pressure-induced thrust force is significantly lower than the prediction based on mere slender-body theory, and to achieve net thrust, one has also to overcome the viscous drag scaling as $1/\sqrt{AR}$ for small aspect ratios.

Acknowledgment

This work was granted access to the HPC resources of IDRIS-France under the allocation A0042A01741 made by GENCI (Grand Equipement National de Calcul Intensif).

References

[1] R. Godoy-Diana, B. Thiria, On the diverse roles of fluid dynamic drag in animal swimming and flying, J. R. Soc. Interface 15 (2018) 20170715. doi:10.1098/rsif.2017.0715.

[2] M. J. Lighthill, Note on the swimming of slender fish, J. Fluid Mech. 9 (1960) 305–317.

[3] M. Triantafyllou, G. Triantafyllou, D. Yue, Hydrodynamics of fishlike swimming, Annu. Rev. Fluid Mech. 32 (2000) 33–53.

[4] J. M. Anderson, K. Streitlien, D. S. Barrett, M. S. Triantafyllou, Oscillating foils of high propulsive efficiency, J. Fluid Mech. 360 (1998) 41–72. doi:10.1017/S0022112097008392.

[5] M. Saadat, F. E. Fish, A. G. Domel, V. Di Santo, G. Lauder, H. Haj-Hariri, On the rules for aquatic locomotion, Phys. Rev. Fluids 2 (2017) 083102. doi:10.1103/PhysRevFluids.2.083102.

[6] M. J. Lighthill, Large-amplitude elongated-body theory of fish locomotion, Proc. R. Soc. Lond. B 179 (1971) 125–138. doi:10.1098/rspb.1971.0085.

[7] U. Ehrenstein, C. Eloy, Skin friction on a moving wall and its implications for swimming animals, J. Fluid Mech. 718 (2013) 321–346. doi:10.1017/jfm.2012.613.

[8] U. Ehrenstein, M. Marquillie, C. Eloy, Skin friction on a flapping plate in uniform flow, Phil. Trans. Roy. Soc. A 372 (2014) 20130345. doi:10.1098/rsta.2013.0345.

[9] M. Piñeirua, B. Thiria, R. Godoy-Diana, Modelling of an acutated elastic swimmer, J. Fluid Mech. 829 (2017) 731–750. doi:10.1017/jfm.2017.302.

[10] G. Lauder, D. Wainwright, A. Fomel, J. Weaver, L. Wen, K. Bertoldi, Structure, biomimetics, and fluid dynamics of fish skin surface, Phys. Rev. Fluids 1 (2016) 060502. doi:10.1103/PhysRevFluids.1.060502.

[11] K. Yanase, P. Saarenrinne, Unsteady turbulent boundary layers in swimming rainbow trout, J. Exp. Biol. 218 (2015) 1373–1385. doi:10.1242/jeb.108083.

[12] D. Floryan, T. Van Buren, C. W. Rowley, A. J. Smits, Scaling the propulsive performance of heaving and pitching foils, J. Fluid Mech. 822 (2017) 386–397. doi:10.1017/jfm.2017.302.

[13] J. H. J. Buchholz, A. J. Smits, The wake structure and thrust performance of a rigid low-aspect-ratio pitching panel, J. Fluid Mech. 603 (2008) 331–365. doi:10.1017/S0022112008000906.

[14] V. Raspa, S. Ramananarivo, B. Thiria, R. Godoy-Diana, Vortex-induced drag and the role of aspect ratio in undulatory swimmers, Phys. Fluids 26 (2014) 041701. doi:10.1063/1.4870254.

[15] J. Aider, J. Beaudoin, J. Wesfreid, Drag and lift reduction of a 3d bluff-body using active vortex generators, Exp. Fluids 48 (2010) 771–789. doi:10.1007/s00348-009-0770-y.

[16] J. Moubogha Moubogha, U. Ehrenstein, J. Astolfi, Forces on a pitching plate: An experimental and numerical study, Appl. Ocean Res. 69 (2017) 27–37. doi:10.1016/j.apor.2017.09.003.

[17] J. Guermond, P. Minev, J. Shen, An overview of a fractional-step method for incompressible flows, Comput. Methods Appl. Mech. Eng. 195 (2006) 6011–6045. doi:10.1016/j.cma.2005.10.010.

[18] R. Shukla, X. Zhong, Derivation of high-order compact finite difference schemes for non-uniform grid using polynomial interplolation, J. Comput. Phys. 204 (2005) 404–429. doi:10.1016/j.jcp.2004.10.014.

[19] A. Quarteroni, A. Valli, Domain decomposition methods for partial differential equations, Oxford, UK: Clarendon Press, 1999.

[20] S. Balay, *et al.*, PETSc users manual, no. ANL-95/11-Revision 3.4 Argonne, IL: Argonne National Laboratory, 2013.

[21] H. Schlichting, Boundary-layer Theory, McGraw-Hill, 1979.

[22] G. K. Batchelor, An Introduction to Fluid Dynamics, Cambridge University Press, 1967.

[23] M. J. Lighthill, Aquatic animal propulsion of high hydromechanical efficiency, J. Fluid Mech. 44 (1970) 265–301.

[24] Y. Yadykin, V. Tenetov, D. Levin, The added mass of a flexible plate oscillating in a fluid, J. Fluids Struct. 17 (2003) 115–123. doi:10.1016/S0889-9746(02)00100-7.

[25] S. Ramananarivo, R. Godoy-Diana, B. Thiria, Passive elastic mechanism to mimic fish-muscle action in anguilliform swimming, J. R. Soc. Interface 10 (2013) 20130667. doi:10.1098/rsif.2013.0667.

[26] M. Piñeirua, R. Godoy-Diana, B. Thiria, Resistive thrust production can be as crucial as added mass mechanisms for inertial undulatory swimmers, Phys. Rev. E 92 (2015) 021001(R). doi:10.1103/PhysRevE.92.021001.

[27] C. Eloy, N. Kofman, L. Schouveiler, The origin of hysteresis in the flag instability, J. Fluid Mech. 691 (2012) 583–593. doi:10.1017/jfm.2011.494.

[28] P. Payne, The virtual mass of a rectangular flat plate of finite aspect ratio, Ocean Engng 8 (1981) 541–545.

[29] C. Eloy, Optimal strouhal number for swimming animals, J. Fluid Struct. 30 (2012) 205–218. doi:10.1016/j.jfluidstructs.2012.02.008.